Spatio-Temporal dMRI Acquisition Design: Reducing the Number of $q\tau$ Samples Through a Relaxed Probabilistic Model

Patryk Filipiak[1], Rutger Fick[1], Alexandra Petiet[2], Mathieu Santin[2], Anne-Charlotte Philippe[2], Stephane Lehericy[2], Rachid Deriche[1], and Demian Wassermann[1]

[1] Université Côte d'Azur - Inria Sophia Antipolis-Méditerranée, France
patryk.filipiak@inria.fr
[2] CENIR - Center for NeuroImaging Research, ICM - Brain and Spine Institute, Paris, France

Abstract. Acquisition time is a major limitation in recovering brain white matter microstructure with diffusion Magnetic Resonance Imaging. Finding a sampling scheme that maximizes signal quality and satisfies given time constraints is NP-hard. We alleviate that by introducing a relaxed probabilistic model of the problem, for which sub-optimal solutions can be found effectively. Our model is defined in the $q\tau$ space, so that it captures both spacial and temporal phenomena. The experiments on synthetic data and *in-vivo* diffusion images of the C57Bl6 wild-type mice reveal superiority of our technique over random sampling and even distribution in the $q\tau$ space.

Keywords: diffusion mri, acquisition design, probabilistic modeling

1 Introduction

Acquisition time is a major limitation in recovering brain white matter microstructure with diffusion Magnetic Resonance Imaging (dMRI). Diving into micro-level details of tissue structure with dMRI requires plenty of scans taken with various acquisition parameters, whereas clinical practice imposes very tight time constraints. We address this problem by proposing an acquisition design that reduces the number of spatio-temporal ($q\tau$) [1] samples under adjustable quality loss.

Sampling the $q\tau$-indexed space efficiently is a non-trivial task. Most current methods assume the fixed τ case, e.g. q-ball imaging [2], diffusion spectrum MRI [3], and multi-shell hybrid diffusion imaging [4]. Nonetheless, direct implementations of these techniques are infeasible in clinical practice due to the requirement of very dense acquisition schemes. Khachaturian et al. [5] alleviated the density demands by introducing Multiple Wavevector Fusion which combined signals from different q-space samples. Another acquisition design that used a semi-stochastic search engine for selecting sub-optimal q-space parameters was

suggested by Koay et al. [6]. Alexander [7] constructed a general framework for experiment design in dMRI that optimized the acquisition parameters aiming at recovery of axon densities and radii in brain white matter. Considerable speed-ups of acquisition process were achieved by Compressed Sensing methods [8] which allowed to reconstruct dMRI signals from undersampled measurements [9–11]. Similarly, functional basis approaches [12–14] allowed for recovering diffusion signal from a relatively small number of q-space samples. Further studies revealed that an introduction of regularization terms for smoothness, sparsity and positivity increased the efficiency of this technique [15]. Moreover, the spatio-temporal model using functional basis approach was proposed recently [16]. For these reasons, we apply the functional basis approach in our $q\tau$-indexed acquisition design study.

Typically, higher density of acquisition assures finer recovery of brain white matter microstructure, although the contributions of particular $q\tau$-indexed samples aren't equal in this respect. In cases where it is possible to perform a dense pre-acquisition prior to a whole study, the optimal acquisition design is reduced to picking the right sub-sampling out of a dense and time-consuming preliminary dMRI scan. In this paper, we show that finding such an optimal subsampling scheme is an instance of the so-called Knapsack Problem (KP) which is NP-hard [17]. We alleviate that by introducing a novel probabilistic model that relaxes the above problem. Then, we apply the Markov Chain Monte Carlo (MCMC) [18] method to obtain the sub-optimal solutions. For modeling the $q\tau$ space, we use the 3D+t framework introduced by Fick et al. [16] with the GraphNet regularization [19] to assure smoothness, sparsity and positivity as suggested in Ref. [15].

We validate our approach on both synthetic diffusion model and real data comprising *in-vivo* diffusion images of the C57Bl6 wild-type mice. The experiments reveal superiority of our technique and efficient reduction of acquisition time to 1/8 of the original time span.

2 Diffusion MRI Theory

We first define the $q\tau$-diffusion signal space and its relationship to the four-dimensional Ensemble Average Propagator (EAP) [1, 20]. In dMRI, the EAP $P(\mathbf{R};\tau)$ describes the probability density that a particle undergoes a displacement $\mathbf{R} \in \mathbb{R}^3$ after diffusion time $\tau \in \mathbb{R}^+$. The EAP is estimated from a set of diffusion-weighted images (DWIs), which are obtained by applying two sensitizing diffusion gradients $\mathbf{G} \in \mathbb{R}^3$ of pulse length δ, separated by separation time Δ. Assuming *narrow pulses*[3] ($\delta \to 0$), we estimate the EAP using an inverse Fourier transform [20] as

$$P(\mathbf{R};\tau) = \int_{\mathbb{R}^3} E(\mathbf{q},\tau) e^{i2\pi \mathbf{q}\cdot\mathbf{R}} d\mathbf{q} \quad \text{with} \quad \mathbf{q} = \gamma\delta\mathbf{G}/2\pi \text{ and } \tau = \Delta - \delta/3, \quad (1)$$

[3] The narrow pulse assumption is most often violated in real-world applications.

where the signal attenuation is given as $E(\mathbf{q},\tau) = S(\mathbf{q},\tau)/S(0,\tau)$ with $S(\mathbf{q},\tau)$ the measured signal at diffusion encoding position $\mathbf{q}$ and diffusion time τ. We denote $q = |\mathbf{q}|$, $\mathbf{q} = q\mathbf{u}$ and $R = |\mathbf{R}|, \mathbf{R} = R\mathbf{r}$, where $\mathbf{u}, \mathbf{r} \in \mathbb{S}^2$ are 3D unit vectors. The wave vector $\mathbf{q}$ on the right side of Eq. (1) is related to pulse length δ, nuclear gyromagnetic ratio γ and the applied diffusion gradient vector $\mathbf{G}$.

3 Methods

A notion of optimality is often subjective and problem-dependent. This section specifies what we consider as an optimal sub-sampling scheme. To this end, we first define the optimization problem in hand. Next, we introduce a probabilistic model that relaxes this problem, and eventually we suggest the sub-optimal problem solver.

3.1 Optimal Acquisition Design

The optimal sub-sampling scheme among the dense pre-acquisition of dMRI is extremely difficult to find. In fact, it requires solving the KP which is NP-hard [17]. Let us remind that the objective of KP is to pick a finite set of items that maximize the total value of the knapsack while respecting its capacity limitation. In our case, the goal is to select a set of $q\tau$ samples that maximize the precision of brain white matter microstructure recovery, while satisfying given time constraints. Assuming the constant acquisition time of each DWI, we express the time budget as the total number of $q\tau$ samples. Next, we define the objective function $F : \{0,1\}^N \rightarrow \mathbb{R}$ in the space of binary vectors $x = (x_1, ..., x_N)$. The assignment $x_i = 1$ for a given $i = 1, ..., N$ indicates that the i-th image from the pool of $N > 0$ DWIs is included in the subset of interest, whereas $x_i = 0$ determines its exclusion. Hence, we aim at solving the following optimization problem

$$\begin{aligned} \arg\min_x F(x) &= \frac{1}{M}\sum_{j=1}^{M} \|E^{(j)} - \hat{E}_x^{(j)}\|_2^2 \\ \text{subject to } \sum_{i=1}^{N} x_i \leq n_{max} \quad &\text{with} \quad 1 \leq n_{max} \leq N-1, \end{aligned} \tag{2}$$

where n_{max} determines the predefined limit of DWIs, $M > 0$ is the number of voxels in each DWI, $E^{(j)}$ is the original signal captured in the j-th voxel with the $q\tau$ measurements, and $\hat{E}_x^{(j)}$ is the corresponding signal reconstructed with x. Note that from now on we will omit the voxel indexing (j) while referring to E and $\hat{E}_x$ in order to simplify notation.

Considering that the optimization problem stated above cannot be solved efficiently, we propose a slightly relaxed probabilistic model instead.

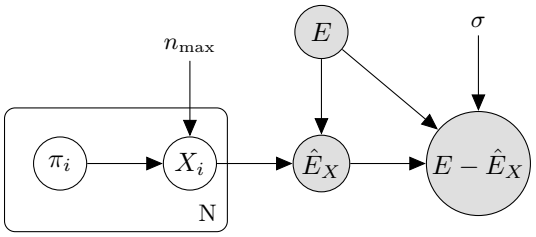

Fig. 1: Graphical model associated with the relaxed probabilistic formulation of the acquisition design. Each variable $X_i \sim B(\pi_i)$ for $\pi_i \sim U[0,1]$ determines inclusion or exclusion of the i-th $q\tau$ sample in obtaining the reconstructed signal $\hat{E}_X$. The residual between $\hat{E}_X$ and the measured signal E is a zero-mean multivariate gaussian. The number of included samples is limited by the constant n_{max}, whereas $E - \hat{E}_X$ is minimized under the level of precision controlled by σ.

3.2 Relaxed Probabilistic Model

We mitigate the binary "inclusion/exclusion" approach in Eq. 2 with probabilities that express how likely it is that given samples are included in the acquisition scheme. Specifically, we define a probabilistic interpretation of the objective square loss function $F(x)$ as the log-likelihood of a multivariate zero-mean Gaussian random variable on the residuals $E - \hat{E}_x$ and rewrite the associated minimization problem from Eq. 2 as

$$\begin{aligned} &\underset{\pi_1,\ldots,\pi_N}{\operatorname{argmin}} \Big(-\log P(E - \hat{E}_X | \pi_1, ..., \pi_N) \Big) \;\propto\; [E - \hat{E}_X]^T \Sigma^{-1} [E - \hat{E}_X] \\ &\Sigma = \sigma^2 \operatorname{Id},\; X \sim (B(\pi_1), \ldots, B(\pi_N)),\; \pi_i \in [0,1], \text{ and a.s. } \sum X < n_{\max}, \end{aligned} \tag{3}$$

where X is an N-vector of Bernoulli-distributed random variables $X_i \sim B(\pi_i)$ with parameters π_i, whereas σ is a tunable parameter specifying the precision of the fitting between E and $\hat{E}_X$. In this setting, the success event of X_i means that the i-th measurement is chosen for our dMRI acquisition sequence. Hence, our decision problem in Eq. 2 is stated as finding $\pi_1, \ldots, \pi_N$ such that $\sum X < n_{max}$ almost surely and $P(E - \hat{E}_X | \pi_1, ..., \pi_N)$ is maximized. When this is achieved, any feasible instance $x \in X$ is considered as a sub-sampling scheme generated by our method. We show the graphical model associated with the above probabilistic formulation of our problem in Fig. 1.

To solve the probabilistic version of the acquisition design problem specified in Eq. 3, we assign uniform distribution to each π_i parameter and we use an MCMC optimiser to find the vector $(\pi_1, \ldots, \pi_N)$ rejecting any sample where $\sum X \geq n_{max}$ to enforce the acquisition time constraint.

Now that we have developed a method to solve our acquisition design problem, we focus on synthesizing the full dMRI signal E from a smaller number of samples by using a regularized functional basis approach.

3.3 $q\tau$-space Model with GraphNet Regularization

We reconstruct the EAP from a finite set of DWIs by representing the discretely measured attenuation $E = E(\mathbf{q}, \tau)$ in terms of the basis coefficients $\mathbf{c}$ of a "Multi-Spherical" 4D $q\tau$-*Fourier* basis [15]. The $q\tau$-basis is formed by the crossproduct of a 3D q-space basis $\Phi_i(\mathbf{q})$ [14] and 1D diffusion time basis $T_j(\tau)$ [16]. The approximated signal attenuation $\hat{E}(\mathbf{q}, \tau, \mathbf{c})$ is given as

$$\hat{E}(\mathbf{q}, \tau, \mathbf{c}) = \sum_{i=1}^{N_\mathbf{q}} \sum_{j=1}^{N_\tau} c_{ij} \Phi_i(\mathbf{q}) T_j(\tau) \quad \text{with} \quad \mathbf{c} = [c_{ij}] \in \mathbb{R}^{N_\mathbf{q} \times N_\tau}, \tag{4}$$

where $N_\mathbf{q}$ and N_τ are the maximum expansion orders of each basis and $\mathbf{c}_{ij}$ weights the contribution of the ij^{th} basis function to $\hat{E}(\mathbf{q}, \tau, \mathbf{c})$. As Φ is a Fourier basis over $\mathbf{q}$, the EAP can be recovered as $\hat{P}(\mathbf{R}; \tau, \mathbf{c}) = \mathrm{IFT}_\mathbf{q}\left[\hat{E}(\mathbf{q}, \tau; \mathbf{c})\right]$.

To estimate $\mathbf{c}$ from a noisy and sparsely sampled $E(\mathbf{q}, \tau)$ we use so-called GraphNet regularization [19]. We impose both signal smoothness using the Laplacian of the reconstructed signal and sparsity in the basis coefficients, while respecting the boundary conditions of the $q\tau$-space.

$$\begin{aligned} \operatorname{argmin}_\mathbf{c} & \overbrace{\iint \left[E(\mathbf{q}, \tau) - \hat{E}(\mathbf{q}, \tau, \mathbf{c})\right]^2 d\mathbf{q} d\tau}^{(1)\text{ Data Fidelity}} + \overbrace{\lambda \iint \left[\nabla^2 \hat{E}(\mathbf{q}, \tau, \mathbf{c})\right]^2 d\mathbf{q} d\tau}^{(2)\text{ Smoothness}} + \overbrace{\alpha \|\mathbf{c}\|_1}^{(3)\text{ Sparsity}} \\ & \text{subject to } E(0, \tau, \mathbf{c}) = 1,\ E(\mathbf{q}, 0, \mathbf{c}) = 1, \end{aligned} \tag{5}$$

The parameters λ, α are the smoothness and sparsity regularization weights, which we optimize using five-fold cross-validation, as suggested by Fick et al. [15]. Such a mechanism for finding the regularization weights assures better overall performance of our acquisition scheme than using fixed values for λ, α (results not presented in this paper).

4 Experiments

The goal of our experiments was to verify if the proposed approach allows to find the sub-sampling scheme that minimizes dMRI signal reconstruction error for a given dense pre-acquisition and a fixed time limit. To this end, we analyzed both synthetic and real diffusion data using the protocol described below.

4.1 Setup

Our initial dense pre-acquisition covered 40 shells, each of which comprised 20 directions and one b_0-image, i.e. $40 \times (20 + 1) = 840$ DWIs in total. We used the b-values ranging from 48 to 7814 s/mm^2 with the separation times Δ between 10 and 20 milliseconds, and the constant gradient duration $\delta = 5$ ms. For each $\tau = \Delta - \delta/3$, we followed the acquisition scheme suggested by Caruyer et al. [21].

For the sub-sampling task, we considered four variants of time limits expressed as budget sizes $n_{max} = \{100, 200, 300, 400\}$ out of 800 DWIs[4]. In order to assure convergence of our MCMC optimizer, we used the fixed number of 10.000 iterations as the termination condition for each run, and we set the level of precision of our model to $\sigma = 0.1$. For comparison, we repeated the same experiments with two alternative sampling schemes. One of them, called *random*, used the uniform distribution of $q\tau$ samples in the index space $\{1, ..., N\}$. In the second one, referred to as *even*, we picked each i-th sample for $i = \lfloor kN/n_{max} \rfloor$ and $k = 1, ..., n_{max}$.

4.2 Objective function & performance measures

The objective of our optimization mechanism was to minimize the mean squared residuals $E - \hat{E}_X$, as discussed earlier in Section 3.2. We used this quantity as a primary measure of microstructure reconstruction accuracy. Additionally, we were interested in verifying how well the temporal phenomena in dMRI signal were preserved while using our scheme. To this end, we studied a set of commonly used spatio-temporal indices [14, 22], namely:

$$\mathrm{RTOP}(\tau, \cdot) = P(0; \tau), \qquad \mathrm{RTPP}(\tau, \cdot) = \int_{\mathbb{R}} \int_{\{\mathbf{r} \in \mathbb{S}^2 : \mathbf{r} \cdot \mathbf{r}_\parallel = 0\}} P(R\mathbf{r}_\perp; \tau) d\mathbf{r}_\perp dR,$$

$$\mathrm{RTAP}(\tau, \cdot) = \int_{\mathbb{R}} P(R\mathbf{r}_\parallel; \tau) dR, \qquad \mathrm{MSD}(\tau, \cdot) = \int_{\mathbb{R}} \int_{\mathbb{S}^2} P(R\mathbf{r}; \tau) R^2 d\mathbf{r} dR,$$

for a given displacement $\mathbf{R} = R\mathbf{r}$, as defined in Section 2. Let us mention that two of the above metrics, i.e. RTAP and RTPP, assume that the white matter is modeled by parallel cylinders with the vectors $\mathbf{r}_\parallel$ parallel and $\mathbf{r}_\perp$ perpendicular to the cylinder axis.

4.3 Diffusion data

In our experiments, we used the following two data sets:

Synthetic data set. In the first scenario, we generated diffusion data using the Watson's dispersed stick model [23] with the concentration parameter $\kappa = 10$. Apart from the original noiseless signal, we also studied the two variants of the signal with incorporated Rician noise, having respective Signal-to-Noise Ratio (SNR) set to 10 and 20.

Real data set. In the second scenario, we used *in-vivo* diffusion images of the corpus callosum of C57Bl6 wild-type mice. Obtaining the initial dense pre-acquisition took approximately 2h10min on an 11.7 Tesla Bruker scanner. The data consists of $96 \times 160 \times 12$ voxels of size $110 \times 110 \times 500$ μm. We manually created a brain mask and corrected the data from eddy currents and motion artifacts using FSL's eddy.

[4] The remaining 40 $b0$-images were excluded from the optimization domain, as they were used by default in every acquisition scheme.

4.4 Results

Tables 1 and 2 summarize the mean squared residuals and the corresponding standard deviations obtained for synthetic and real diffusion data, respectively. Each value is averaged over 50 sub-sampling schemes obtained with a given technique[5].

We compared all the pairs of outputs using paired two-sample Student's t-tests with the Bonferroni adjusted significance level $\alpha = 10^{-8}$ and the number of degrees of freedom $2n - 2 = 98$. The results that were statistically significantly better then the peer approaches are printed in bold in Tables 1 and 2. As we can see, our approach outperformed the *even* and *random* sub-sampling schemes in almost all of the cases. However, in some cases with $n_{max} > 200$, no approach was significantly better then the other two.

Figures 2 and 3 illustrate the reconstruction of the spatio-temporal indices RTOP, RTAP, RTPP, MSD $\pm$ 1 standard deviation, with $n_{max} = 100$, obtained for the synthetic and real diffusion data, respectively. The black plots show reference curves, whereas the colored plots represent *random* (green), *even* (blue) and *ours* (red) sub-sampling schemes.

Finally, Figure 4 illustrates a sample acquisition scheme obtained with our method for the Watson's dispersed stick with SNR=20. The main orientation of the sticks is plotted with the red line. The black dots represent q-space locations. The sizes of dots are proportional to the magnitudes of gradient G.

5 Discussion

Acquisition time matters, especially in the long-lasting processes like dMRI. In this paper, we show that contributions of particular $q\tau$-indexed samples to the recovery level of tissue microstructure aren't equal. As a result, the straightforward sub-sampling schemes like *even* or *random* are outperformed by our approach that minimizes the tissue microstructure reconstruction error. Also, by defining the optimal acquisition design in Equation 2, we proved that an optimal sub-sampling scheme is extremely difficult to find. On the other hand, our relaxed probabilistic model allowed us to localize sub-optimal solutions after 10.000 iterations of an MCMC optimizer.

5.1 Our approach largely reduces acquisition time

The performance of our method was best observed under the tightest considered budget size, i.e. $n_{max} = 100$. This simple remark opens the field for the future studies in this area. The superiority of the proposed acquisition scheme over the *random* and *even* sub-sampling schemes gives the opportunity to apply our approach in the clinical practice. Indeed, reducing the acquisition time to 1/8 or

[5] Except for the *even* sub-sampling scheme which is deterministic with respect to n_{max}, i.e. always outputs the same scheme for a given budget size, so there was no need to repeat the experiment more than once.

noise level	budget $n_{\max}$	(MSE ± STD) $\times 10^4$ ours	rand	even	NRMSE $\times 10^3$ ours	rand	even
noiseless signal	100	$\mathbf{2.4 \pm 0.12}$	5.9 ± 4.88	4.1	25.0	39.1	32.6
	200	$\mathbf{1.2 \pm 0.01}$	1.9 ± 2.65	1.8	17.4	22.1	21.6
	300	0.7 ± 0.01	0.8 ± 0.15	0.7	13.5	14.3	13.3
	400	0.6 ± 0.02	0.6 ± 0.10	0.7	12.7	12.9	13.3
SNR=20 (Rician)	100	$\mathbf{6.7 \pm 0.28}$	10.0 ± 2.59	11.4	41.1	50.5	53.8
	200	$\mathbf{4.1 \pm 0.09}$	5.4 ± 0.66	7.0	32.4	37.1	42.1
	300	$\mathbf{3.5 \pm 0.08}$	4.2 ± 0.31	3.9	29.9	32.5	31.3
	400	$\mathbf{3.4 \pm 0.06}$	3.6 ± 0.27	3.6	29.4	30.2	30.4
SNR=10 (Rician)	100	$\mathbf{25.5 \pm 4.84}$	29.1 ± 5.05	40.0	80.4	86.0	100.8
	200	$\mathbf{17.0 \pm 0.30}$	18.9 ± 1.60	22.9	65.7	69.2	76.3
	300	$\mathbf{14.6 \pm 0.34}$	16.8 ± 1.20	17.6	60.9	65.3	66.8
	400	14.6 ± 0.15	15.1 ± 0.81	15.2	60.9	61.9	62.1

Table 1: Summary of residuals $E - \hat{E}_X$ presented as the mean squared errors (MSE) with the corresponding standard deviations (STD) and the normalized root mean squared errors (NRMSE) for the Watson's dispersed stick model either with or without Rician noise, under the time limits expressed as budget sizes $n_{max} = 100, ..., 400$ out of 800 densely acquired samples. The MSEs printed in bold are statistically significantly better than the peer approaches, assuming $p < 10^{-8}$. Our sampling scheme outperforms the other two in almost all cases.

region of interest	budget $n_{\max}$	(MSE ± STD) $\times 10^4$ ours	rand	even	NRMSE $\times 10^3$ ours	rand	even
CC genu	100	$\mathbf{40.2 \pm 0.47}$	43.5 ± 1.43	44.9	114.3	118.9	120.8
	200	$\mathbf{35.8 \pm 0.13}$	37.1 ± 0.74	40.0	107.9	109.8	114.1
	300	$\mathbf{33.5 \pm 0.14}$	34.8 ± 0.51	34.9	104.4	106.4	106.5
	400	$\mathbf{32.9 \pm 0.15}$	33.3 ± 0.33	33.4	103.4	104.1	104.1
CC body	100	$\mathbf{48.8 \pm 0.25}$	52.3 ± 2.45	62.4	137.4	142.1	155.3
	200	$\mathbf{39.1 \pm 0.37}$	42.7 ± 1.17	58.0	122.9	128.4	149.7
	300	$\mathbf{35.8 \pm 0.24}$	38.1 ± 1.09	39.9	117.7	121.4	124.1
	400	$\mathbf{34.2 \pm 0.35}$	35.3 ± 0.70	37.2	114.9	116.8	119.9
CC splenium	100	$\mathbf{42.3 \pm 0.31}$	47.2 ± 2.25	58.3	111.7	117.9	131.1
	200	$\mathbf{37.9 \pm 0.52}$	39.8 ± 0.97	67.4	105.7	108.4	141.0
	300	37.3 ± 0.17	36.8 ± 0.53	36.9	104.8	104.2	104.4
	400	35.3 ± 0.24	35.2 ± 0.36	36.5	102.0	101.9	103.8

Table 2: Summary of residuals $E - \hat{E}_X$ presented as the mean squared errors (MSE) with the corresponding standard deviations (STD) and the normalized root mean squared errors (NRMSE) for the three regions of C57Bl6 wild-type mouse corpus callosum (CC), under the time limits expressed as budget sizes $n_{max} = 100, ..., 400$ out of 800 densely acquired samples. The MSEs printed in bold are statistically significantly better than the peer results, assuming $p < 10^{-8}$. Our sampling scheme outperforms the other two in almost all cases.

2/8 of the original time span, just like in the case presented in this paper, allows for huge savings while minimizing the imposed quality loss.

What is also interesting, the differences between the three analyzed sub-sampling schemes were decreasing as the budget size increased. This leads to the conclusion that optimization of the acquisition scheme plays an important role only in the cases where time limitations are the highest.

All the three tested approaches scored similar results in the noiseless synthetic cases. However, the addition of noise turned *even* sub-sampling scheme into the least effective one among the analyzed methods, whereas it increased the

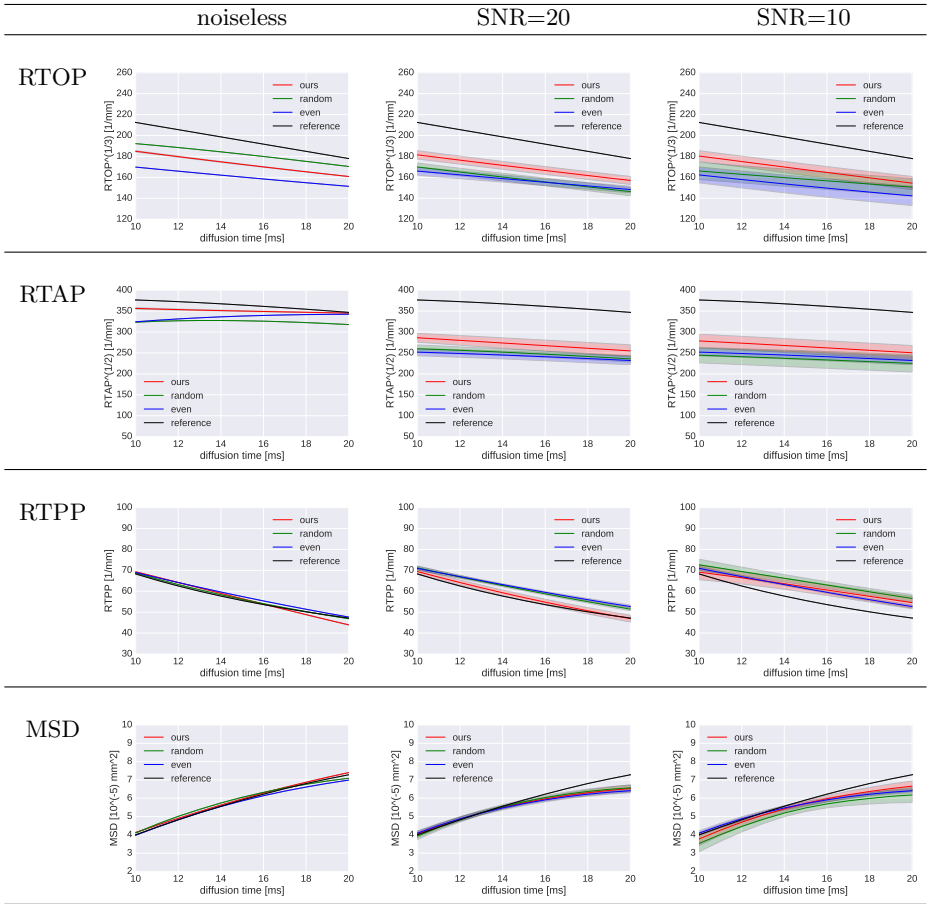

Fig. 2: Reconstruction of spatio-temporal indices RTOP, RTAP, RTPP, MSD $\pm$ 1 standard deviation with $n_{max} = 100$, obtained for the Watson's dispersed stick model either with or without Rician noise. The black plots show reference curves, the colored plots represent *random* (green), *even* (blue) and *ours* (red) sub-sampling schemes. Our approach resulted in the most exact estimations of indices (the red curves lie nearest the black ones) in almost all cases.

superiority of our scheme over the other two. It is most probably due to the ability of GraphNet regularization to decrease the impact of the noise in a signal. As a result, our approach was able to assure much lower residuals in most of the cases with noisy data, while *even* approach remained very sensitive to noise.

5.2 Spatio-temporal phenomena are preserved in our scheme

We mentioned earlier that our optimization mechanism targeted the signal reconstruction only. Nonetheless, the spatio-temporal phenomena measured with the analyzed $q\tau$ indices were preserved even for $n_{max} = 100$, as illustrated in Figures 2 and 3.

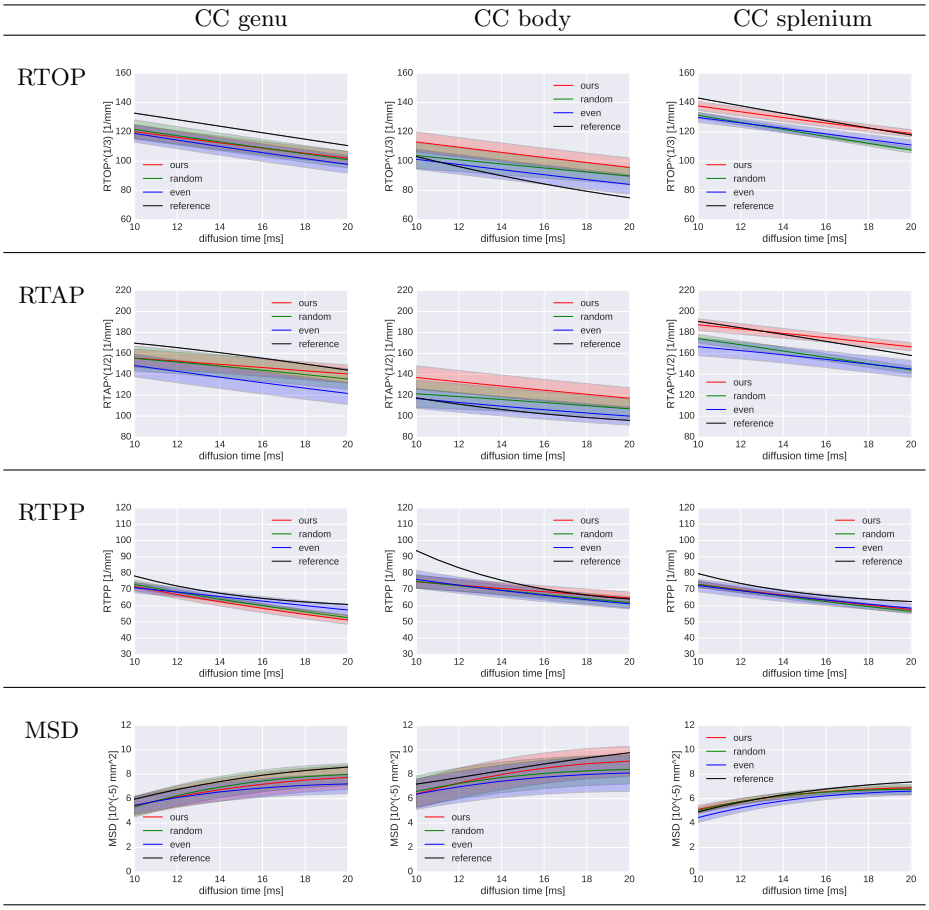

Fig. 3: Reconstruction of spatio-temporal indices RTOP, RTAP, RTPP, MSD ± 1 standard deviation with $n_{max} = 100$, obtained for the three regions of C57Bl6 wild-type mouse corpus callosum (CC). The black plots show reference curves, the color plots represent *random* (green), *even* (blue) and *ours* (red) sub-sampling schemes.

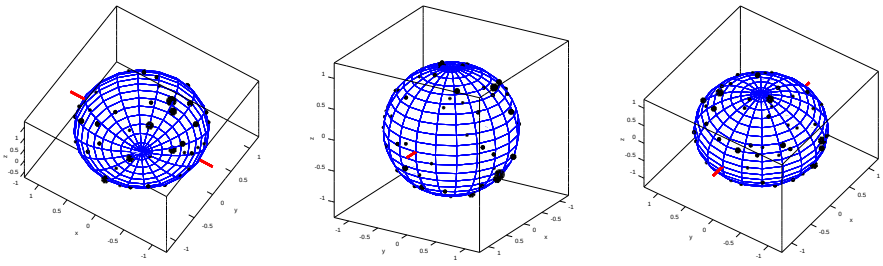

(a) (b) (c)

Fig. 4: Sample acquisition scheme obtained with our method for the Watson's dispersed stick with SNR=20. The main orientation of the sticks is plotted with the red line. The black dots represent q-space locations. The sizes of dots are proportional to the magnitudes of gradient G. Note that the regions located perpendicular to the main orientation of sticks are covered most densely and the G-values are the highest there. On a contrary, the regions located parallel to the orientation are covered more loosely and the G-values are visibly lower.

Our approach produced the best estimations of $q\tau$ indices (the red curves lie nearest the black ones in Figure 2) in most of the cases with synthetic diffusion data. However, RTOP and RTAP were visibly underestimated, particularly in the noisy data cases, which apparently requires future improvements in this regard. On the other hand, RTPP and MSD were well reconstructed by all the three methods, either with or without the presence of noise in the signal.

Unlike the synthetic case, most of the results obtained for the real data set are readably more dispersed. It is also more difficult to tell, which approach outperforms the others. Finally let us note that the reference curves, taken from the dense pre-acquisition, are inevitably perturbed by a measurement noise, which makes comparison even more complicated in this case. By observing the plots in Figure 3, we conclude that the $q\tau$ indices are generally preserved, although less exactly than for the synthetic data set.

We believe that incorporating a mechanism for fitting spatio-temporal phenomena into the objective function will successfully address the discrepancies stated in this section.

5.3 The acquisition scheme that we obtained is reasonable

The sample acquisition scheme, presented in Figure 4, gives us an impression of what an optimized sub-sampling looks like. Note that the regions located perpendicular to the main orientation of sticks are covered most densely and the G-values are the highest there. On a contrary, the regions located parallel to the orientation are covered more loosely and the G-values are visibly lower. We claim that such a scheme coincides with an intuition of optimal spatial locations of sub-samples.

6 Conclusions

We proposed the spatio-temporal dMRI acquisition design that greatly reduces the number of $q\tau$ samples under the adjustable quality loss. Despite the fact that selecting a sampling scheme that maximizes brain white matter reconstruction accuracy and satisfies given time constraints is NP-hard, our relaxed probabilistic model allowed to find sub-optimal solutions effectively.

The experiments on both synthetic diffusion data and real *in-vivo* DWIs of the C57Bl6 wild-type mice revealed superiority of our technique over random sub-sampling and even distribution in the $q\tau$ space. Our approach performed best under the tightest among all the considered time constraints, leading to reduction of acquisition time to 1/8 of the original time span.

In this study, we assumed availability of a densely acquired dMRI signal for reference, although it is not often the case. Future work should target the reproducibility of our approach among different subjects and scanners. Also, the optimizer itself might be improved to assure faster convergence and adaptability, and thus achieve lower average quality loss of solutions.

Acknowledgements

This work has received funding from the ANR/NSF award NeuroRef; the European Research Council (ERC) under the Horizon 2020 research and innovation program (ERC Advanced Grant agreement No 694665 : CoBCoM); the MAXIMS grant funded by ICM's The Big Brain Theory Program and ANR-10-IAIHU-06.

References

1. Callaghan, P.T.: Pulsed-gradient spin-echo nmr for planar, cylindrical, and spherical pores under conditions of wall relaxation. Journal of magnetic resonance, Series A **113**(1) (1995) 53–59
2. Tuch, D.S.: Q-ball imaging. MR in medicine **52**(6) (2004) 1358–1372
3. Wedeen, V.J., Hagmann, P., Tseng, W.Y.I., Reese, T.G., Weisskoff, R.M.: Mapping complex tissue architecture with diffusion spectrum magnetic resonance imaging. Magnetic resonance in medicine **54**(6) (2005) 1377–1386
4. Wu, Y.C., Field, A.S., Alexander, A.L.: Computation of diffusion function measures in q-space using magnetic resonance hybrid diffusion imaging. IEEE transactions on medical imaging **27**(6) (2008) 858–865
5. Khachaturian, M.H., Wisco, J.J., Tuch, D.S.: Boosting the sampling efficiency of q-ball imaging using multiple wavevector fusion. MR in Med. **57**(2) (2007) 289–296
6. Koay, C.G., Özarslan, E., Johnson, K.M., Meyerand, M.E.: Sparse and optimal acquisition design for diffusion MRI and beyond. Med. Ph. **39**(5) (2012) 2499–2511
7. Alexander, D.C.: A general framework for experiment design in diffusion mri and its application in measuring direct tissue-microstructure features. Magnetic Resonance in Medicine **60**(2) (2008) 439–448
8. Donoho, D.L.: Compressed sensing. IEEE Tr. inf. theory **52**(4) (2006) 1289–1306
9. Lustig, M., Donoho, D., Pauly, J.M.: Sparse mri: The application of compressed sensing for rapid mr imaging. MR in medicine **58**(6) (2007) 1182–1195

10. Merlet, S., Deriche, R.: Compressed sensing for accelerated EAP recovery in diffusion MRI. In: MICCAI. (2010) 1–14
11. Saint-Amant, E., Descoteaux, M.: Sparsity characterisation of the diffusion propagator. In: Proc. Intl. Soc. Mag. Reson. Med. Volume 19. (1915) 2011
12. Descoteaux, M., Angelino, E., Fitzgibbons, S., Deriche, R.: Regularized, fast, and robust analytical q-ball imaging. MR in Medicine **58**(3) (2007) 497–510
13. Assemlal, H.E., Tschumperlé, D., Brun, L.: Efficient and robust computation of pdf features from diffusion mr signal. Medical image analysis **13**(5) (2009) 715–729
14. Özarslan, E., Koay, C.G., Shepherd, T.M., Komlosh, M.E., İrfanoğlu, M.O., Pierpaoli, C., Basser, P.J.: Mean apparent propagator (MAP) MRI: A novel diffusion imaging method for mapping tissue microstructure. NeuroImage **78** (2013) 16–32
15. Fick, R., Petiet, A., Santin, M., Philippe, A.C., Lehericy, S., Deriche, R., Wassermann, D.: Multi-spherical diffusion mri: Exploring diffusion time using signal sparsity. In: MICCAI 2016 Workshop on Computational dMRI (CDMRI'16). (2016)
16. Fick, R., Wassermann, D., Pizzolato, M., Deriche, R.: A unifying framework for spatial and temporal diffusion in diffusion MRI. In: International Conference on Information Processing in Medical Imaging, Springer (2015) 167–178
17. Hochbaum, D.S.: Approximation algorithms for NP-hard problems. PWS (1996)
18. Gilks, W.R., Richardson, S., Spiegelhalter, D.: Markov chain Monte Carlo in practice. CRC press (1995)
19. Grosenick, L., Klingenberg, B., Katovich, K., Knutson, B., Taylor, J.E.: Interpretable whole-brain prediction analysis with GraphNet. NeuroImage (2013)
20. Stejskal, E.: Use of spin echoes in a pulsed magnetic-field gradient to study anisotropic, restricted diffusion and flow. The Journal of Chemical Physics **43**(10) (1965) 3597–3603
21. Caruyer, E., Lenglet, C., Sapiro, G., Deriche, R.: Design of multishell sampling schemes with uniform coverage in diffusion MRI. Magnetic resonance in medicine **69**(6) (2013) 1534–1540
22. Fick, R.H., Wassermann, D., Caruyer, E., Deriche, R.: MAPL: Tissue microstructure estimation using Laplacian-regularized MAP-MRI and its application to HCP data. NeuroImage **134** (2016) 365–385
23. Kaden, E., Knosche, T., Anwander, A.: Parametric. NeuroImage **37** (2007) 474–488